Published in final edited form as:
IEEE J Sel Top Appl Earth Obs Remote Sens. 2018 December ; 11(12): 4578–4590. doi:10.1109/jstars.2018.2865251.

Spatial and temporal variability of root-zone soil moisture acquired from hydrologic modeling and AirMOSS P-band radar

Wade T. Crow,
USDA ARS Hydrology and Remote Sensing Laboratory, Beltsville, MD, USA.

Sushil Milak,
USDA ARS Hydrology and Remote Sensing Laboratory, Beltsville, MD, USA and SSAI, Lanham, MD, USA.

Mahta Moghaddam,
University of Southern California, Los Angeles, CA, USA.

Alireza Tabatabaeenejad,
University of Southern California, Los Angeles, CA, USA.

Sermsak Jaruwatanadilok,
Jet Propulsion Laboratory, California Institute of Technology, Pasadena, CA, USA.

Xuan Yu,
Depart. of Geological Science, University of Delaware, Newark, DE, USA.

Yuning Shi,
Depart. of Ecosystem Science and Management, Pennsylvania State University, University Park, PA, USA.

Rolf H. Reichle,
NASA Goddard Space Flight Center, Global Model and Assimilation Office, Greenbelt, MD, USA.

Yutaka Hagimoto,
Oregon State University, Corvallis, OR, USA.

Richard H. Cuenca
Oregon State University, Corvallis, OR, USA.

Abstract

The accurate estimation of grid-scale fluxes of water, energy, and carbon requires consideration of sub-grid spatial variability in root-zone soil moisture (RZSM). The NASA Airborne Microwave Observatory of Subcanopy and Subsurface (AirMOSS) mission represents the first systematic attempt to repeatedly map high-resolution RZSM fields using airborne remote sensing across a range of biomes. Here we compare 3-arc-sec (~100-m) spatial resolution AirMOSS RZSM retrievals from P-band radar acquisitions over 9 separate North American study sites with analogous RZSM estimates generated by the Flux-Penn State Hydrology Model (Flux-PIHM). The two products demonstrate comparable levels of accuracy when evaluated against ground-

wade.crow@ars.usda.gov.

based soil moisture products and a significant level of temporal cross-correlation. However, relative to the AirMOSS RZSM retrievals, Flux-PIHM RZSM estimates generally demonstrate much lower levels of spatial and temporal variability, and the spatial patterns captured by both products are poorly correlated. Nevertheless, based on a discussion of likely error sources affecting both products, it is argued that the spatial analysis of AirMOSS and Flux-PIHM RZSM fields provide meaningful upper and lower bounds on the potential range of RZSM spatial variability encountered across a range of natural biomes.

Index Terms—

Soil moisture; hydrologic modelling; radar remote sensing and spatial scaling

I. Introduction

WHILE considerable advances have been made in the global, coarse-scale (>10 km) retrieval of surface (top 5-cm) soil moisture [1–3], our ability to measure fine-scale (~100 m) soil moisture variations beyond the near-surface remains relatively limited [4–5]. Due to the significant amount of fine-scale spatial variability typically found in soil moisture fields [6–7], and the nonlinear relationship between root-zone soil moisture and water-limited fluxes of water, energy, and carbon between the land surface and the atmosphere, this shortcoming has significant implications for our ability to model large-scale variations in the Earth's water, energy, and carbon cycles.

At a minimum, accurate statistical descriptions of sub-grid soil moisture variability are needed to specify the correct grid-scale relationship between soil moisture and grid-scale fluxes [8–10]. The accurate representation of fine-scale soil moisture patterns is also important for capturing surface saturation connectively patterns governing streamflow generation [11], the design of ground validation protocols for satellite soil moisture products [12], the implementation of high-resolution modeling for precision agriculture [13], and the assimilation of fine-scale, ground-based soil moisture observations into regional drought monitors [14]. Unfortunately, these applications are currently limited by a lack of reliable information concerning the statistical variability of fine-scale root-zone soil moisture patterns.

The application of L- (0.5 to 1.5 GHz) and C-band (4 to 8 GHz) radar and radiometry on airborne platforms is well-established and can be used to derive high-resolution soil moisture imagery (see e.g., [15]). However, as with satellite platforms, airborne measurements at these wavelengths are limited to providing soil moisture estimates for only a thin surface soil layer (on the order of 2- to 5-cm deep), which is not directly reflective of deeper, vertically-integrated soil moisture values that drive variations in vegetation stomatal conductance (that, in turn, regulate surface fluxes of water, energy, and carbon within water-limited, vegetated landscapes). The most viable approach for the remote retrieval of high-resolution root-zone soil moisture is currently P-band (250- to 500-MHz) radar. In particular, P-band backscatter observations contain soil moisture information for the top few decimeters of the soil column and therefore provide much deeper vertical sampling than 5-cm soil

moisture estimates derived from higher-frequency C- and L-band microwave remote sensing [4, 16]. Hereinafter the term “root-zone soil moisture” (RZSM) will be applied to vertically averaged, volumetric [$m^3\ m^{-3}$] soil moisture values within the top 40-cm of the soil column. Note that the usage of the term does not imply that vegetation roots are present in only (or throughout) the 0- to 40-cm soil layer (see additional discussion in Section II).

From 2012 to 2015, the NASA Airborne Microwave Observatory of Subcanopy and Subsurface (AirMOSS) mission successfully deployed a P-band radar on an airborne platform over a variety of North American biomes [16]. The mission leveraged synthetic aperture radar (SAR) processing to produce 3-arc-sec (~100-m) P-band backscatter imagery of 10 North American study sites. Level 1 backscatter products acquired at each site were processed into a Level 2/3 RZSM data product (hereinafter “AirMOSS L2/3”). These retrievals provide RZSM information at an unprecedented combination of spatial extent, temporal coverage, vertical sampling depth, and horizontal resolution.

Paralleling the development of soil moisture remote sensing technologies has been the growth of high-resolution (30–100 m), spatially-distributed, three-dimensional hydrologic models (ostensibly) capable of capturing RZSM spatial variability at a comparable set of spatial scales [17]. These models explicitly represent the lateral flow of water due to topographic forcing. Since topographic variability can usually be captured in high-resolution digital elevation models (DEMs), they capture at least a fraction of the processes governing the high-resolution distribution of soil moisture across natural landscapes. When forced with high-resolution land cover and soil texture products, they can also capture RZSM patterns arising from fine-scale spatial variations in soil hydraulic parameters and vegetation characteristics. However, efforts to independently validate RZSM fields generated by high-resolution models have generally yielded mixed results. While some modelling studies appear successful in replicating observed soil moisture variability (see e.g., [7]), others suggest that models systematically underestimate such variability [18]. However, as discussed below, such verification is difficult. Here, we will focus on RZSM results generated by one such model, the Flux-Penn State Integrated Hydrologic Model (Flux-PIHM) [19].

These two approaches, high-resolution 3-D hydrologic modeling and airborne-based P-band radar remote sensing, represent (arguably) the only two credible means of estimating spatially-continuous RZSM fields at fine spatial resolutions. While the temporal characteristics of both approaches can be evaluated against individual point-scale observations (see, e.g. results presented in Section III.A below), existing ground-based soil moisture networks generally do not provide the required combination of dense spatial sampling and large-scale extent required to fully validate spatial predictions made by either product [12]. As a result, the only viable evaluation strategy for spatially-distributed RZSM information provided by modeling and P-band remote sensing (over large spatial extents) lies in their mutual comparison. To the best of our knowledge, such comparisons have not yet been described in the literature. Below we attempt to fill this gap by comparing the temporal and spatial variations of 3-arc-sec (~100 m) RZSM fields acquired from both Flux-PIHM modeling and AirMOSS remote sensing retrievals.

Section II provides background information on both approaches and the AirMOSS study sites. RZSM time and space variability comparisons are presented in Section III, discussed in Section IV, and summarized in Section V.

II. Data and Approach

The AirMOSS mission deployed a P-band synthetic aperture radar on a NASA Gulfstream-3 aircraft. The instrument imaged fully polarimetric (HH, VV, HV, and VH) backscatter over a ~25 km × ~100 km rectangular mosaic area containing each of the study sites shown in Figure 1. Since the goal of the mission was an improved estimate of North American net ecosystem exchange of carbon between the land surface and atmosphere, study sites were chosen specifically to represent a broad range of North American biomes.

Nine AirMOSS sites are considered here: (1) the Tonzi Ranch site (TZ) in central California, (2) the Metolius site in eastern Oregon (OR), (3) the Marena Oklahoma Soil Moisture Active Passive (SMAP) In Situ Testbed (MOISST) site in central Oklahoma (OK), (4) the Howland (HW) Forest site in Maine, (5) the Harvard Forest (HF) site in Massachusetts, (6) the Duke Forest (DF) site in North Carolina, (7) the Chamela (CH) site in Mexico, (8) the Boreal Ecosystem Research and Monitoring Sites (BERMS) forest (BF) site in Saskatchewan, and (9) the Walnut Gulch site in southeastern Arizona (AZ). AirMOSS science flights started in August 2012 and finished in September 2015 after logging more than 1200 total flight hours. See Table 1 for a complete list of over flights conducted at each site.

Two separate algorithms were employed to convert AirMOSS L1 HH and VV backscatter imagery into a 3 arc-sec (~100-m) AirMOSS L2/3 retrieved RZSM product [20]. The first, hereinafter referred to as the “University of Southern California” or “USC” algorithm, was designed for single-species forests and lightly vegetated grassland/savannas landcover present in the TZ, OR, BF, AZ, and OK sites. The second, referred to as the “Jet Propulsion Laboratory” or “JPL” approach was designed specifically to handle mixed-forest land cover and applied at the HW, HF, DF, and CH sites. Since each algorithm was applied only to sites containing (suitable) land surface conditions for which it was designed, no cross-comparison results are available. However, additional details for both algorithms are given below.

Both AirMOSS L2/3 algorithms retrieve a vertically-continuous soil moisture profile. AirMOSS RZSM results discussed below are based on the vertical integration of these profiles within the top 40 cm of the soil column. As noted above, the use of this terminology does not imply that all plant roots are contained within this vertical layer. Instead, a 40-cm depth was selected to correspond (roughly) to the maximum validation depth of AirMOSS L2/3 RZSM retrievals (see Section III.A below).

A. The USC AirMOSS L2/3 RZSM Retrieval Algorithm

To model the radar response over the TZ, OR, BF, WG and OK sites, the USC AirMOSS L2/3 RZSM retrieval algorithm employs a discrete-scatterer model which assumes a single-species forest with horizontal homogeneity within a radar pixel while allowing for vertical heterogeneity by introducing a trunk layer and a canopy layer [21, 22]. The trunk layer is represented by vertical dielectric cylinders, and the canopy layer contains randomly

distributed large and small dielectric cylinders representing branches. Leaves in the canopy layer are represented by disks (for deciduous forests) or cylinders (for coniferous forests) and are assumed to be randomly distributed throughout the canopy. The radar model calculates the total backscattered power as the sum of the power from several contributing mechanisms, namely: (1) scattering from the crown layer, (2) scattering from trunks, (3) double-bounce scattering between the crown layer and the ground, (4) double-bounce scattering between trunks and the ground, and (5) backscattering from the ground (where the ground is modeled as homogeneous layers of soil).

The soil moisture profile is assumed to be the only unknown in the corresponding retrieval algorithm. Other parameters characterizing the radar pixel (i.e., soil texture, vegetation parameters and structural information) are considered known as ancillary data layers. The vertical soil moisture profile is assumed to have the quadratic form $az^2 + bz + c$, where z [m] is the depth within the soil column, and the coefficients a, b and c are depth-constant unknowns to be retrieved [20].

Note that the retrieval of these three unknowns based on two backscatter observations (HH and VV) makes the inverse problem ill-posed. Accordingly, upper and lower bounds are defined for each unknown coefficient based on available in-situ soil moisture data at each corresponding AirMOSS site [20,23]. A simulated annealing algorithm adapted from [24] is then used to minimize a cost function based on the difference between measured and calculated backscattering coefficients. Due to specific AirMOSS system properties (including attenuation of P-band signals, observed signal-to-noise ratio, system noise floor, and calibration accuracy), a 45-cm validity depth is assumed for formal verification performed at the BF, OR, OK, TZ, and WG sites [20]. For additional validation details, see Section III.A below and [20].

B. The JPL AirMOSS L2/3 RZSM Retrieval Algorithm

The two-step JPL AirMOSS L2/3 RZSM retrieval algorithm was applied to retrieve RZSM for mixed-forest land cover conditions existing at the HF, HW, DF, and CH AirMOSS sites. First, vertically averaged soil moisture, above ground biomass, and surface roughness heights were simultaneously estimated using a Levenberg-Marquardt nonlinear least-squares optimization method. Second, vertically averaged soil moisture was converted into a vertically distributed soil moisture profile. The Levenberg-Marquardt method is a nonlinear, least-squares curve fitting approach defined here by:

$$S(W, \varepsilon, s) = \Sigma_{i=1}^{n} \left[\sigma_{pq_i} - f(W, \varepsilon, s)\right]^2 \quad (1)$$

where σ_{pq_i} is the polarimetric backscattering radar cross-section coefficient; W is the above-ground biomass; ε is the dielectric constant of the ground, and s is the root-mean-squared height of the ground surface roughness. The optimization procedure was based on the minimization of the distance S between AirMOSS-observed backscatter values and a forward-scattering model.

The forward model is a simplified radar backscattering coefficient based on fitting a physical-scattering mechanism to the data. It consists of three backscattering terms: (1) “direct”, (2) “direct reflect”, and (3) “ground” where the direct term is scattering from the crown and trunk of tress; direct reflect is the double-bounce scattering interaction between trees and the ground, and the ground term is the direct scattering from the ground. These three terms sum to equal the total polarimetric cross-section:

$$\sigma_{pq} = (\text{direct}) + (\text{direct reflect}) + (\text{ground}) \tag{2}$$

and are parameterized as:

$$\text{direct} = A_{pq} W^{\alpha_{pq}} \cos\theta \left(1 - \exp\left[-\frac{B_{pq} W^{\beta_{pq}}}{\cos\theta}\right]\right) \tag{3}$$

$$\text{direct reflect} = C_{pq} W^{\delta_{pq}} \sigma_{pq} \sin\theta \left(\exp\left[-\frac{B_{pq} W^{\beta_{pq}}}{\cos\theta}\right]\right) \tag{4}$$

$$\text{ground} = S_{pq} \left(\exp\left[-\frac{B_{pq} W^{\beta_{pq}}}{\cos\theta}\right]\right) \tag{5}$$

where $\sigma_{pq} = |R_{pq}|^2(\exp[-4k^2s^2\cos^2\theta])$ [–]; W is biomass [Mg/ha]; R_{pq} is the Fresnel reflection coefficient of the ground for polarization pq; pq denotes polarization which can be VV, HH, HV, or VH; s is the root-mean-square height of the rough ground [m]; k is the wave number [m^{-1}]; θ is the radar incidence angle, and S_{pq} is the scattering cross-section from the rough ground using [25]. The coefficients α, β, and δ are polarization-dependent shape coefficients which depend on tree geometry parameters such as trunk height and diameter, branch length and diameter, and leaf size/density. Likewise, the coefficients A, B, and C are polarization-dependent weights which determine the relative and absolute contribution of (3–5). Here these coefficients were determined using previously obtained data which matches with ground observations/measurements.

The second step of the JPL RZSM algorithm was the retrieval of the soil moisture profile. This was based on a look-up table approach where polarimetric backscattering coefficients were pre-computed based on vertically distributed soil texture information. The solution was the profile candidate associated with the closest fit to the observed backscattering coefficients. For further details, see [26].

C. The Flux-Penn State Integrated Hydrologic Model

The Penn State Integrated Hydrologic Model (PIHM) is a multi-process, multi-scale hydrologic model where major hydrological processes are fully coupled using a semi-discrete finite volume method [27–28]. For channel routing and overland flow, which is governed by the St. Venant equations, both the kinematic and diffusion wave approximations are included. For saturated groundwater flow, the 2-D Dupuit approximation is applied. For

unsaturated flow, two options can be applied: 1) a 1-D vertically integrated form of Richards equation or 2) a shallow groundwater assumption in which unsaturated soil moisture is dependent on groundwater level.

The original soil water balance for PIHM has recently been modified. In the new model version, renamed “Flux-PIHM”, the original PIHM unsaturated-saturated zone soil water balance is coupled with vertical soil water flux processes taken from the Noah land surface model [29] to redistribute soil moisture across multiple soil layers [19, 23]. See Figure 2 for a diagram of Flux-PIHM water and energy flux processes. Note that flow within the unsaturated zone remains 1-D (vertical-only), while 2-D (i.e., lateral flow) aspects of Flux-PIHM are confined to the saturated zone.

For our Flux-PIHM application, four soil layers with (spatially-fixed) depths of: 0–10 cm, 10–40 cm, 40–100 cm, and 100–200 cm were utilized, and RZSM results were based on the weighted averaging of the top two Flux-PIHM soil layers to obtain an integrated 0–40 cm RZSM value. For cases in which the total soil depth (to bedrock) was deeper than 200 cm, an additional soil layer was added. Meteorological inputs into Flux-PIHM consisted of hourly precipitation, air temperature, relative humidity, wind velocity, solar radiation, longwave radiation, and air pressure observations. For sites in the United States, this data was obtained from the hourly North American Land Data Assimilation Version 2 (NLDAS-2) forcing dataset [30]. Local tower-based meteorology observations and topographic corrections to solar radiation, precipitation, and air temperature were also used. For sites outside of the NLDAS-2 domain (i.e., BR and CH), baseline forcing data at hourly, 0.50° × 0.67° (latitude by longitude) resolution were acquired from the Modern-Era Retrospective analysis for Research and Applications (MERRA) with gauge-corrected precipitation taken from the MERRA-Land product (based on the daily, 0.5° Climate Prediction Center (CPC)-Global-Unified rain gauge analysis) [31].

Pedologic, topographic, geologic, and vegetation parameters (e.g., leaf area index, aerodynamic roughness length, and a vegetation canopy interception storage factor) for Flux-PIHM were derived from a 30-m United States Geologic Survey digital elevation model (DEM), a bedrock elevation map, the Soil Survey Geographic Database (SSURGO) soil texture classification [32], and the National Land Cover Database (NLCD) 2011 land cover classification [33]. Watershed delineation, stream definition and the horizontal variations in the depth of constraining layers were based on the DEM and bedrock map. These maps were then ingested into the PIHMgis tool [34] to obtain a fixed triangulated irregular network (TIN) mesh for each site. The mean size of TIN elements was constrained to the range 100^2–300^2 m^2. Parameter lookup tables were defined to assign physical parameters to individual TIN elements based on characteristics identified in these maps. Specifically, Flux-PIHM requires vertical soil hydraulic conductivity, porosity, residual porosity, horizontal area fraction of macro-pore, vertical area fraction of macro-pore, macro-pore depth, macro-pore horizontal hydraulic conductivity, macro-pore vertical hydraulic conductivity, and the van Genuchten alpha and beta parameters [35].

As noted above, baseline values for these parameters were based on the SSURGO soil classification. However, whenever possible, such values were updated using local in situ soil

texture and hydraulic parameter measurements. In particular, limited soil water retention point data available at select sites were incorporated into the Rosetta model [36] to provide improved estimates of soil hydraulic parameters. Nevertheless, the uncertainty in these numerous horizontal and vertical physical parameters for any given site is impossible to quantify. Limited model calibration was also performed on a site-by-site basis to select soil hydraulic properties optimizing model predictions of stream flow for specific storm events in 2012 and 2013. Note that the Flux-PIHM calibration did not use the ground-based soil moisture observations described in Section II.D thereby ensuring the validity of the validation results presented below. Flux-PIHM simulations were initialized from uniform conditions on 01 January 2009 and spun-up for nearly four years until the start of AirMOSS data collection in late 2012.

The spatial domain of Flux-PIHM simulated was defined as a series of closed hydrologic basins (with sizes on the order of 100–1000 km^2) selected to maximize overlap with AirMOSS over-flight coverage (see Figure 3). Nevertheless, spatial discrepancies remain between the Flux-PIHM modeling domain and AirMOSS spatial coverage (see Figure 3b). Therefore, all statistics sampled below are based solely on areas of overlapping Flux-PIHM and AirMOSS L2/3 coverage.

D. Ground Observations

As noted above, our primary aim is the comparison of AirMOSS and Flux-PIHM RZSM estimates at the AirMOSS sites. However, we will also review validation results against a set of independent, ground-based soil moisture observations collected within the BF, TZ, DF, HW, CH, and OR sites. Each instrumented site consisted of one so-called “super profile” station, which included instrumentation for a full radiation balance and soil heat flux, in addition to the instrumentation for profile soil water content, soil water tension, soil temperature, and precipitation. Each site also had two standard profiles which had the same instrumentation as the super site for profile soil water content, soil water tension, soil temperature (including soil surface temperature measured by thermal infrared), and precipitation. The three profiles were generally on a linear transect emanating from the flux tower with the super profile located approximately 50 m from the tower and with 50-m spacing between the other monitored profiles. An attempt was made to place the profiles such that they captured the anticipated range of soil water content at the site due to vegetation and topographic effects. The design of the profile monitoring scheme was intended to measure the profile soil water content, soil water tension, and soil temperature from the surface to a depth of 1 m with higher vertical resolution towards the surface. Soil water content and soil temperature were measured continuously every 5 minutes and soil water tension every 20 minutes. For more details and information on sensor installation and calibration, see [23].

III. Results

Figure 3a and 3b show example Flux-PIHM and AirMOSS L2/3 RZSM imagery for each AirMOSS ground site. As discussed above, each product is posted on a fixed 3-arc-sec (~100 m) grid defined within each of the study sites. The spatial extent of the AirMOSS

L2/3 retrievals at each of the nine sites (Figure 3b) is determined by the ~25 km × ~100 km AirMOSS flight pattern developed at each site. The precision platform autopilot system on the NASA Gulfstream-3 airplane housing AirMOSS ensured that flight lines were flown within the same 10-m tube on every over-flight of each site.

The remainder of this section is sub-divided as follows. Section III.A reviews the evaluation of Flux-PIHM and AirMOSS RZSM predictions using the ground-based soil moisture observations described in Section II.D. Following that, Sections III.B and III.C compares the representation of RZSM temporal and spatial variability provided by AirMOSS and Flux-PIHM.

A. Ground Validation of AirMOSS and Flux-PIHM RZSM

Even a cursory glance at Figure 3 reveals the presence of large differences between AirMOSS and Flux-PIHM RZSM estimates. The ground-based soil moisture observations described in Section II.D provide an opportunity to independently assess the accuracy of AirMOSS L2/3 and Flux-PIHM RZSM across time at a series of point-scale ground measurement sites. AirMOSS L2/3 validation results have been published previously. At the BF, OR, AZ, OK, and TZ study sites, [20, 37] reported that 0–25 cm and 0–45 cm soil moisture products acquired from AirMOSS L2/3 soil moisture profile retrievals had a root-mean-square-error (RMSE) of 0.050 m^3m^{-3} and 0.063 m^3m^{-3}, respectively, when evaluated point-by-point against the ground-based soil moisture observations described in Section II.D.

Comparable validation comparisons can be made for Flux-PIHM soil moisture estimates. Figure 4 compares 0–10 cm, 10–40 cm, and 40–100 cm Flux-PIHM soil moisture estimates to corresponding ground-based observations acquired within the BF, DF, HF, TZ, CH, and OR sites. To maximize consistency with AirMOSS results reported above, Flux-PIHM results are shown only for hourly time steps corresponding to AirMOSS overpass times listed in Table 1. Results demonstrate that vertically integrated soil moisture estimates obtained directly from Flux-PIHM's 0–10 cm, 10–40 cm, and 40–100 cm soil layers have a RMSE accuracy of 0.052 m^3m^{-3}, 0.053 m^3m^{-3}, and 0.067 m^3m^{-3}, respectively, when compared against ground-based soil moisture observations. Therefore, validation against independent, point-scale observations suggests that the RMSE accuracy of 0–40 cm RZSM estimates obtained from AirMOSS and Flux-PIHM are roughly comparable. Note that comparisons are limited to only a sub-set of AirMOSS sites (TZ, OR, HF, DF, CH and BF) where ground-based soil moisture instrumentation was installed during AirMOSS campaigns [23].

B. Temporal Variability

Figure 5 plots scene-average spatial means for both Flux-PIHM and AirMOSS RZSM fields where each symbol represents a spatially averaged RZSM value for a single AirMOSS over-flight (see Table 1) acquired at a single study site (see Figure 1). Plotted spatial means are based on sampling all 3-arc-sec pixels containing a valid RZSM estimate in both products. A modest, yet statistically significant, amount of temporal correlation (0.37 [–], $p < 0.05$ [–]) is

found. However, larger systematic differences emerge when directly comparing RZSM estimates across a broader range of temporal and spatial scales.

For example, a substantial portion of the correlation in Figure 5 is attributable to strong spatial variability *between* study sites (due to bulk climate and land cover differences) as opposed to pure temporal variability *within* a single site. To better isolate the degree of spatially-fixed, temporal correlation, Figure 6 plots time series correlations between Flux-PIHM and AirMOSS L2/3 RZSM imagery at a 3-arc-sec grid scale. Correlations (R) are calculated only for grid cells containing at least 10 days of common AirMOSS and Flux-PIHM coverage. The R value shown above each image give the scene-averaged correlation (i.e., temporal correlations calculated at the 3-arc-sec scale and then spatially averaged). Note that, due to a lack of adequate temporal sampling, no correlation results are shown for the CH site. At the TZ, OR, OK, and DF sites, fine-scale temporal correlations are modest (i.e., in the range 0.20 to 0.50 [–]) but remain broadly positive. In contrast, more pronounced areas of negative temporal correlation are found at the HW, HF, BF, and AZ sites.

Figure 7a plots the temporal standard deviation of scene-scale RZSM for both AirMOSS and Flux-PIHM. AirMOSS L2/3 predicts higher levels of temporal variability in scene-scale means than Flux-PIHM for all sites except for TZ and OR. This overall low bias in Flux-PIHM RZSM temporal variability (relative to AirMOSS L2/3) is apparent at all spatial scales at which the products can be sampled. For example, Figure 7b plots scene-averaged values for 3-arc-sec temporal standard deviations calculated at each site (i.e., sampled in time at the 3-arc-sec scale and then spatially-averaged into a single scene-scale mean). Results are closely analogous to Figure 7a and demonstrate a tendency for Flux-PIHM to predict lower temporal variability at both spatial scales. Note that the sites with the lowest AirMOSS/Flux-PIHM RZSM temporal correlation in Figure 6 are among the three sites with the lowest Flux-PIHM temporal variability in Figure 7 (HF, BF and AZ). This suggests that one factor underlying the lack of time-series correlation in Figure 6 is low temporal variability in Flux-PIHM RZSM estimates.

As noted above, the two exceptions to the low bias in Flux-PIHM temporal variability are the TZ and OR sites. Both sites are characterized by a Mediterranean climate with cool, wet winters and warm, dry summers. They therefore exhibit very strong soil moisture seasonality (since seasonal periods of low potential evaporation occur concurrently with periods of high rainfall and vice versa). Figures 8a and 8b plot time series for both the scene-scale mean and the within-scene spatial standard deviation of 3-arc-sec Flux-PIHM and AirMOSS L2/3 RZSM estimates at times corresponding to AirMOSS over-flights. The mean time series for Flux-PIHM soil moisture results in TZ and OR reflect seasonal patterns expected in a Mediterranean climate (i.e., high RZSM during the winter and spring and low RZSM in the summer and fall). This pronounced seasonality drives the large temporal standard deviations observed at these sites in Figure 7 and the relatively robust temporal correlations between Flux-PIHM and AirMOSS RZSM estimates seen in Figure 6. In contrast, while the AirMOSS L2/3 RZSM retrievals demonstrate a comparable amount of temporal variability at the OR site, they lack the same coherent seasonal cycle (Figures 8b). More absolute agreement between the AirMOSS and Flux-PIHM results is found at the TZ site (Figure 8a), where the overall magnitude and the seasonal characteristics of soil moisture temporal

variability is consistent between AirMOSS and Flux-PIHM. However, TZ and OR time series results in Figures 8a and 8b are not generally representative for the broader range of sites that do not experience a Mediterranean climate. Time series results at the DF (Figure 8f) and AZ (Figure 8i) are somewhat more typical in that they are characterized by relatively little temporal variation in Flux-PIHM results which is sharply contrasted by much stronger variability in scene-averaged AirMOSS L2/3 results. Note that strong temporal variability in AirMOSS L2/3 results) may be artificially inflated by time-varying retrieval errors may (particularly at the DF site in Figure 8f).

C. Spatial Variability

The uniqueness of the Flux-PIHM and AirMOSS products lies in their ability to represent multi-scale spatial variability in RZSM. Figure 9 plots the sampled spatial standard deviation of AirMOSS and Flux-PIHM RZSM fields at spatial resolutions ranging between 3 and 30 arc-sec (~100 m to ~1,000 m). To avoid the spurious impact of spatial data gaps on sampling, only grid cells containing a complete set of sub-grid 3-arc-secs AirMOSS and Flux-PIHM estimates are re-sampled to progressively coarser spatial resolutions. This ensures that AirMOSS L2/3 and Flux-PIHM RZSM spatial statistics calculated at all resolutions contain the same spatial support.

At the finest sampling resolution (3-arc-sec), AirMOSS RZSM retrievals have higher spatial variability than comparable Flux-PIHM RZSM estimates for seven of the nine AirMOSS sites. The first exception is at the OR site. As shown in Figure 8b, high amounts of 3-arc-sec RZSM spatial variability occur in Flux-PIHM as the OR site during the wet winter due to a strong east-west gradient in wintertime precipitation patterns captured within by NLDAS-2 rainfall data (see Figure 3b for an example of this). This, in turn, produces a large spatial standard deviation in the Flux-PIHM RZSM simulations at the site. It is possible that these large-scale patterns accurately reflect actual orographic rainfall variations at the site [38]. However, these patterns do not manifest themselves in AirMOSS L2/3 RZSM retrievals (see Figure 3a) – and may simply be an artifact of error in the spatial pattern of NLDAS-2 rainfall forcing data at this site. The second exception occurs within the BF site. Here both AirMOSS and Flux-PIHM predict exceptionally low RZSM spatial variability ($< 0.04\ m^3m^{-3}$ see Figures 9) and almost no temporal dynamics (Figures 8e). This suggests that this site is atypical with respect to its degree of time/space soil moisture variability.

This spatial variability gap between AirMOSS and Flux-PIHM is reduced somewhat by re-sampling to spatial resolutions coarser than 10 arc-sec (~300 m). Nevertheless, AirMOSS L2/3 RZSM estimates generally retain more spatial variability up to a resolution scale of about 30 arc-sec (~1,000 m). The only site where aggregation changes the qualitative relationship between AirMOSS and Flux-PIHM RZSM variability is BF. Here, Flux-PIHM RZSM spatial variability is dominated by large-scale (~10-km) soil texture patterns while AirMOSS L2/3 RZSM manifests itself on much finer spatial scales (see Figure 3b). Consequently, spatial aggregation up to 300-m has a much stronger (reducing) impact on AirMOSS L2/3 spatial variability.

The impact of soil moisture variability on nonlinear grid-scale fluxes can also depend on higher-order moment for sub-grid scale soil moisture distributions [9]. Therefore, it is useful

to consider the scaling of higher-order moments for AirMOSS and Flux-PIHM RZSM spatial distributions. Figure 10 shows the spatial skewness (i.e., the third statistical moment about the mean for a given field normalized by the cube of its standard deviation) across a range of spatial resolution scales (analogous to Figure 9). At a 3-arc-sec scale, spatial skewness differences between AirMOSS and Flux-PIHM RZSM results are frequently large and often extend to disagreements regarding the overall sign of sampled skewness (see TZ, BF, and AZ results in Figure 10). At best, spatial aggregation leads to only slight convergence in AirMOSS L2/3 and Flux-PIHM RZSM skewness results.

Finally, Figure 11 examines the degree to which spatial variability in Flux-PIHM RZSM fields correlates with that of AirMOSS RZSM retrievals. Plotted values represent the time average (across all AirMOSS over-flight times listed in Table 1) of Flux-PIHM versus AirMOSS spatial correlation results sampled individually for each individual AirMOSS overpass time. As such, it describes pure spatial correlation existing between the two RZSM products. Note that this contrasts with the purely temporal correlations captured in Figure 6. As in Figures 9 and 10, spatial averaging is performed prior to the correlation calculation to resample RZSM fields to progressively coarser spatial resolutions and examine the impact of such averaging on sampled spatial correlations. Overall, sampled spatial correlations between the two products are quite low. Assessing the statistical significance of correlation results in Figure 11 is complicated by the large amount of temporal and spatial auto-correlation present in both the Flux-PIHM and the AirMOSS L2/3 RZSM fields. Nevertheless, the marginal levels of correlation seen in Figure 11 (always < 0.20 [–] and often negative) provide little evidence that co-located AirMOSS and Flux-PIHM RZSM estimates contain common spatial features.

IV. Discussion

The observed contrast in Flux-PIHM and AirMOSS temporal variability statistics (see Figure 7) is not entirely unexpected. It is well-known that soil moisture products acquired via different estimation approaches (e.g., modeling, remote sensing, and *in situ* measurements) tend to exhibit significant systematic differences with regards to their temporal statistics [39–41].

Likewise, the general underestimation of RZSM spatial variability by Flux-PIHM is also not surprising. Model-based estimates of soil moisture rely heavily on the characterization of heterogeneity within dynamic (e.g., precipitation) and static (e.g., topographic position) model forcing data sets to capture soil moisture spatial variability. Therefore, known spatial inadequacies (e.g., non-resolved soil texture variability or the coarse-resolution representation of rainfall) in these forcing data sets will generally result in an overly smoothed spatial representation of soil moisture fields [42]. In such cases, the true spatial resolution of a model-based RZSM product may be coarser than the spatial scale of its fundamental computational elements (i.e., model grid cells or TINs). While an attempt has been made to force Flux-PIHM with the highest-quality and highest-resolution inputs available, this tendency is almost certainly present in the spatially distributed Flux-PIHM results presented here. Likewise, soil moisture variability is known to arise from a variety of

topographic, pedologic, and vegetative processes – not all of which are explicitly captured by Flux-PIHM (see Figure 2).

Therefore, *a priori*, there are credible reasons to suspect that Flux-PIHM will tend to underestimate the magnitude of fine-scale spatial variability in RZSM. This suspicion is consistent with existing Flux-PIHM validation results against dense ground-based soil moisture networks. For example, [18] found that Flux-PIHM underestimated the spatial variability of 10-cm soil moisture when evaluated against spatially dense soil moisture monitoring sites located within a very small 0.08 km^2 watershed.

In contrast to the "bottom-up" approach applied in hydrologic models, AirMOSS L2/3 retrievals are based on a "top-down" approach whereby a highly variable backscatter field is processed to separate out an underlying soil moisture signal from other spatially-varying geophysical features (e.g., vegetation, topography, soil texture, and surface roughness). Given that the parameterization of backscatter responses arising from these features is approximate in both AirMOSS L2/3 RZSM retrieval algorithms (see Section II), it is possible that spatial patterns in AirMOSS RZSM L2/3 retrievals reflect variability present in these ancillary fields. Likewise, synthetic aperture radar backscatter products are commonly impacted by residual amounts of uncorrelated spatial noise or "speckle." While every attempt has been made to minimize these effects in the AirMOSS L2/3 retrieval process, it seems reasonable to assume that, if anything, AirMOSS L2/3 retrievals will tend to overestimate fine-scale soil moisture variability.

Based on this reasoning, comparisons between AirMOSS L2/3 and Flux-PIHM estimates of multi-scale RZSM spatial variability presented in Figure 9 likely represent valid upper and lower bounds, respectively, for the true multi-scale magnitude of RZSM soil moisture variability. Since the nonlinearity of relationships between soil moisture and surface fluxes means that grid-scale fluxes are sensitive to the presence (or absence) of sub-grid RZSM spatial variability [9, 43], such bounds are valuable for defining appropriate coarse-scale soil moisture/flux relationships for land surface models.

Clearly, a third source of independent, spatially variable, RZSM data would be valuable as an arbiter of whether AirMOSS or Flux-PIHM provides a less biased estimate of RZSM spatial variability. Unfortunately, the spatial scales of existing, long-term data sets derived from the point-scale observations are typically not well-suited for the replication of Figure 9 using ground observations. These networks lack either adequate spatial sampling to estimate soil moisture on a ~100-m spatial scale or sufficient spatial coverage to acquire enough ~100-m pixels to provide an adequate sample of spatial variability. Triple collocation validation strategies [44] could potentially be applied to better distribute errors between Flux-PIHM, AirMOSS L2/3 and ground-based soil moisture estimates. However, this would not address the spatial limitations of the ground-based observations. In addition, it would require a much more temporally extensive AirMOSS data record.

Therefore, results here underscore the need to develop new ground-based soil moisture measurement techniques capable of resolving RZSM at a broader range of spatial resolution and extent scales. Notable efforts in this direction include the innovative use of: wireless

sensor networks [45] and passive cosmic ray sensors [46] in ground-based soil moisture networks. The further development and deployment of these approaches could conceivably provide an enhanced source of ground-truth information to arbitrate the significant contrast between modeled and remotely-sensed RZSM estimates found here.

V. Summary

AirMOSS and Flux-PIHM RZSM fields both demonstrate reasonable levels of skill in reproducing temporal variations in independent, ground-based RZSM estimates acquired at a point (Figure 4). Likewise, they exhibit a modest level of temporal correlation between their areal-mean (Figure 5) and between their 3-arc-sec (~100-m) RZSM estimates (Figure 6). However, the two products differ in their characterization of temporal and spatial variability in RZSM fields. Flux-PIHM, for example, generally predicts lower levels of temporal variability than AirMOSS (Figure 7) apart from sites (i.e., OR and TZ) with a Mediterranean climate where Flux-PIHM temporal variability is enhanced via its (presumably accurate) representation of strong RZSM seasonal variability (Figures 8a and 8b). AirMOSS L2/3 RZSM estimates are also generally more spatially variable than comparable Flux-PIHM predictions (Figure 9). Moreover, there is very little demonstrated linear consistency between time-static spatial RZSM patterns estimated by both approaches (Figure 11).

Due to the nonlinear nature of land model physics, and the importance of sub-grid soil moisture connectivity for runoff generation, uncertainty in the magnitude of sub-grid RZSM variability has significant consequences for the derivation of appropriate grid-scale relationships between RZSM and land surface water, energy, and carbon fluxes. While this work only scratches the surface in terms of resolving this uncertainty, it does provide, for the first time, defensible bounds on RZSM spatial variability within a critical ~100-m to ~1,000-m scale range (Figure 9).

It should also be noted that land data assimilation approaches exist for integrating remotely-sensed and model-based RZSM estimates into a unified analysis. Within the AirMOSS project, a data assimilation approach was applied to generate the AirMOSS Level 4 RZSM product [47] based on the integration of AirMOSS L2/3 into Flux-PIHM. However, limitations in the temporal frequency of AirMOSS L2/3 retrievals restricted this effort to the use of a highly simplified assimilation approach. Increased temporal frequency in the availability of remotely-sensed RZSM estimates would allow for the application of more complex data assimilation approaches such as the Ensemble Kalman filter currently used to generate the SMAP Level 4 Surface and Root-zone Soil Moisture product [48]. By contributing to our understanding of the spatial characteristics of errors in remotely-sensed and model-based RZSM estimates, Figures 9 and 10 will aid in the design of such systems [49].

In addition to data assimilation, alternative remote sensing retrieval and model calibration approaches that can potentially reduce the contrasts between the Flux-PIHM and AirMOSS L2/3 RZSM results. For example, Flux-PIHM underestimation of RZSM spatial variability is likely linked to the calibration strategy employed to parameterize Flux-PIHM. Following

typical practice, Flux-PIHM parameters were calibrated here using only streamflow observations. However, [50] demonstrate that the spatial accuracy of fine-scale Flux-PIHM RZSM estimates can be improved if multivariate observations (including RZSM) are utilized for calibration. Likewise, the accuracy of remotely sensed AirMOSS L2/3 RZSM retrievals can be further improved by applying physics-based constraints during the RZSM retrieval [51]. Future work along either of these two paths would likely reduce the RZSM variability contrasts observed here.

Acknowledgments

This work was supported by the National Aeronautics and Space Administration Earth Ventures Sub-Orbital-1 Program (AirMOSS mission). Additional resources supporting this work were provided by the NASA High-End Computing (HEC) Program through the NASA Advanced Supercomputing (NAS) Division at Ames Research Center. Parts of this research was carried out at the Jet Propulsion Laboratory, California Institute of Technology, under a contract with the National Aeronautics and Space Administration.

References

[1]. Entekhabi D et al., “The Soil Moisture Active and Passive (SMAP) Mission,” Proceedings of the IEEE, vol. 98, no. 5, pp. 704–716, 10.1109/JPROC.2010.2043918, 2010.

[2]. Kerr Y et al., “Overview of SMOS performance in terms of global soil moisture monitoring after six years in operation,” Rem. Sens. Environ, vol. 180, pp. 40–63, 10.1016/j.rse.2016.02.042, 2016.

[3]. Chan S et al., “Assessment of the SMAP Passive Soil Moisture products,” IEEE Trans. Geosci. Remote Sens, vol. 54, pp. 4994–5007, 10.1109/TGRS.2016.2561938, 2016.

[4]. Moghaddam M et al., “Microwave Observatory of Subcanopy and Subsurface (MOSS): A Mission Concept for Global Deep Soil Moisture Observations,” IEEE Transactions on Geoscience and Remote Sensing, vol. 45, no. 8, pp. 2630–2643, 10.1109/TGRS.2007.898236, 2007.

[5]. Hain CR, Crow WT, Anderson MC, and Mecikalski JR, “An EnKF dual assimilation of thermal-infrared and microwave satellite observations of soil moisture into the Noah land surface model,” Water Resources Research, vol. 48, W11517, 10.1029/2011WR011268, 2012.

[6]. Famiglietti JS, Ryu D, Berg AA, Rodell M, and Jackson TJ, “Field observations of soil moisture variability across scales,” Water Resour. Res, vol. 44, W01423, 10.1029/2006WR005804, 2008.

[7]. Chaney NW, Roundy JK, Herrera-Estrada JE, and Wood EF, “High-resolution modeling of the spatial heterogeneity of soil moisture: Applications in network design,” Water Resour. Res, vol. 51, pp. 619–638, doi:10.1002/2013WR014964, 2015.

[8]. Nykanen DK, and Foufoula-Georgiou E, “Soil moisture variability and scale-dependency of nonlinear parameterizations in coupled land–atmosphere models,” Advances in Water Resources, vol. 24, no. 9–10, pp. 1143–1157, 10.1016/S0309-1708(01)00046-X, 2001.

[9]. Crow WT, and Wood EF, “The value of coarse-scale soil moisture observations for regional surface energy balance modeling,” Journal of Hydrometeorology, vol. 3, pp. 467–482, 2002.

[10]. Bronstert A, and Bárdossy A, “The role of spatial variability of soil moisture for modelling surface runoff generation at the small catchment scale,” Hydrology Earth System Science, vol. 3, 10.5194/hess-3-505-1999, 1999.

[11]. Western AW, Bloschl G, and Grayson RB, “Towards capturing hydrologically significant connectivity in spatial patterns,” Water Resources Research, vol. 37(1), pp. 83–97, 2001.

[12]. Crow WT, Berg AA, Cosh MH, Loew A, Mohanty BP, Panciera R, de Rosnay P, Ryu D, and Walker JP, “Upscaling sparse ground-based soil moisture observations for the validation of coarse-resolution satellite soil moisture products,” Reviews of Geophysics, vol., 50, RG2002, 10.1029/2011RG000372, 2012.

[13]. Ge Y, Thomasson JA, and Sui R, “Remote sensing of soil properties in precision agriculture: A review,” Front. Earth Sci, vol. 5, no. 229, 10.1007/s11707-011-0175-0, 2011.

[14]. Gruber A, Crow WT, “The potential of 2D Kalman filtering for soil moisture data assimilation,” Rem. Sens. Environ, vol. 171, pp. 137–148, 10.1016/j.rse.2015.10.019, 2015.

[15]. Colliander A, Chan S, Kim S, Das N, Yueh S, Cosh M, Bindlish R, Jackson T, and Njoku E, “Long term analysis of PALS soil moisture campaign measurements for global soil moisture algorithm development,” Rem. Sens. Environ vol 121, pp. 309–322, 10.1016/j.rse.2012.02.002, 2012.

[16]. Moghaddam M, Tabatabaeenejad A, Chen RH, Saatchi SS, Jaruwatanadilok S, Burgin M, Duan X, and Truong-Loi ML, AirMOSS: L2/3 Volumetric Soil Moisture Profiles Derived From Radar, 2012–2015, ORNL DAAC, Oak Ridge, Tennessee, USA, 10.3334/ORNLDAAC/1418, 2016.

[17]. Wood EF et al., “Hyper-resolution global land surface modeling: Meeting a grand challenge for monitoring Earth’s terrestrial water,” Water Resour. Res, vol. 47, W05301, 10.1029/2010WR010090, 2011.

[18]. Shi YC, Baldwin DC, Davis KJ, Yu X, Duffy CJ, and Lin H, “Simulating high resolution soil moisture patterns in the Shale Hills catchment using a land surface hydrologic model,” Hydrological Processes, vol. 29, pp. 4624–4637, 10.1002/hyp.10593, 2015.

[19]. Shi YC, Davis KJ, Duffy CJ, and Yu X, “Development of a coupled land surface hydrologic model and evaluation at a critical zone observatory,” Journal of Hydrometeorology, vol. 14, pp. 1401–1420, 10.1175/JHM-D-12-0145.1, 2013.

[20]. Tabatabaeenejad A, Burgin M, and Moghaddam M, “P-band radar retrieval of subcanopy and subsurface soil moisture profile as a second order polynomial: First AirMOSS results,” IEEE Trans. Geosci. Remote Sens, vol. 53, no. 2, pp. 645–658, 2015.

[21]. Durden SL, Van Zyl JJ, and Zebker HA, “Modeling and observation of the radar polarization signature of forested areas,” IEEE Trans. Geosci. Remote Sens, vol. 27, no. 3, pp. 290–301, 1989.

[22]. Burgin M, Clewley D, Lucas RM, and Moghaddam M, “A generalized radar backscattering model based on wave theory for multilayer multispecies vegetation,” IEEE Trans. Geosci. Remote Sens, vol. 49, no. 12, pp. 4832–4845, 2011.

[23]. Cuenca RH, Hagimoto Y, Ring TM, and Beamer JP, “Interpretation of In Situ observations in support of P-band radar retrievals,” IEEE Journal of Selected Topics in Applied Earth Observations and Remote Sensing, vol. 9, no. 7, pp. 3122–3130, 2016.

[24]. Corana A, Marchesi M, Martini C, and Ridella S, “Minimizing multimodal functions of continuous variables with the ‘Simulated Annealing’ algorithm,” ACM Trans. Math. Softw, vol. 13, no. 3, 262–280, 1987.

[25]. Oh Y, Sarabandi K, and Ulaby FT, “An empirical model and an inversion technique for radar scattering from bare soil surfaces,” IEEE Trans. Geosci. Remote Sens, vol. 30, no. 2, pp. 370–381, 3 1992.

[26]. Truong-Loï ML, Saatchi SS, and Jaruwatanadilok S, “Soil moisture estimation under tropical forests using UHF radar polarimetry,” IEEE Transactions on Geoscience and Remote Sensing,” vol. 53, no. 4, pp. 1718–1727. 10.1109/TGRS.2014.2346656, 2015.

[27]. Qu Y, and Duffy CJ, “A semidiscrete finite volume formulation for multiprocess watershed simulation,” Water Resour. Res, vol. 43, W08419, 10.1029/2006WR005752, 2007.

[28]. Kumar M, Toward a hydrologic modeling system, PhD dissertation, 251 pp., The Pa. State Univ., 2009.

[29]. Ek MB, Mitchell KE, Lin Y, Rogers E, Grunmann P, Koren V, Gayno G, and Tarpley JD, “Implementation of Noah land surface model advances in the National Centers for Environmental Prediction operational mesoscale Eta model,” J. Geophys. Res, 108, 8851, 10.1029/2002JD003296, D22, 2003.

[30]. Xia Y et al., NLDAS Primary Forcing Data L4 Hourly 0.125 × 0.125 degree V002, Greenbelt, Maryland, USA, Goddard Earth Sciences Data and Information Services Center (GES DISC), Accessed May 2017, 10.5067/6J5LHHOHZHN4, 2009.

[31]. Reichle RH, Koster RD, De Lannoy GJM, Forman BA, Liu Q, Mahanama SPP, and Toure A, “Assessment and enhancement of MERRA land surface hydrology estimates,” Journal of Climate, vol. 24, pp. 6322–6338, 10.1175/JCLI-D-10-05033.1, 2011.

[32]. Soil Survey Staff, Natural Resources Conservation Service, United States Department of Agriculture. Soil Survey Geographic (SSURGO) Database, Available online, Accessed September 2014.

[33]. Homer CG, Dewitz JA, Yang L, Jin S, Danielson P, Xian G, Coulston J, Herold ND, Wickham JD, and Megown K, "Completion of the 2011 National Land Cover Database for the conterminous United States-Representing a decade of land cover change information," Photogrammetric Engineering and Remote Sensing, vol. 81, no. 5, pp. 345–354, 2015.

[34]. Bhatt G, Kumar M, and Duffy CJ, "A tightly coupled GIS and distributed hydrologic modeling framework," Environ. Modell. Software, vol. 62, pp. 70–84, 2014.

[35]. van Genuchten MT, "A closed-form equation for predicting the hydraulic conductivity of unsaturated soils," Soil Science Society of America Journal, vol. 44(5), pp. 892–898, 10.2136/sssaj1980.03615995004400050002x, 1980.

[36]. Schaap GS, Leij FJ, and van Genuchten MT, "Rosetta: a computer program for estimating soil hydraulic parameters with hierarchical pedotransfer functions," Journal of Hydrology, vol. 251, pp. 163–176, 2001.

[37]. Tabatabaeenejad A, Chen R, and Moghaddam M, "Assessment of retrieval errors of AirMOSS root-zone soil moisture products," Proc. IGARSS'16, Beijing, China, 7 2016.

[38]. Smith RB, Barstad I, and Bonneau L, "Orographic precipitation and Oregon's climate transition," Journal of the Atmospheric Sciences," vol. 62, pp. 177–191, 10.1175/JAS-3376.1, 2004.

[39]. Yu X, Duffy C, Kaye J, Crow W, Bhatt G, Shi Y, and Lakshmi V, "Watershed reanalysis of water and carbon cycle models at a critical zone observatory," Remote sensing of the terrestrial water cycle, John Wiley & Sons, Hoboken, NJ, pp. 493–509, 2014.

[40]. Reichle RH, Koster RD, Dong J, and Berg AA, "Global soil moisture from satellite observations, land surface models, and ground data: Implications for data assimilation," Journal of Hydrometeorology, vol. 5, pp. 430–442, 2004.

[41]. Drusch M, Wood EF, and Gao H, "Observation operators for the direct assimilation of TRMM microwave imager retrieved soil moisture," Geophys. Res. Lett, vol. 32, L15403, 10.1029/2005GL023623, 2005.

[42]. Peters-Lidard CD, Pan F, Wood F, "A re-examination of modeled and measured soil moisture spatial variability and its implications for land surface modeling," Advances in Water Resources, vol. 24, no. 9–10, pp. 1069–1083, 2001.

[43]. Crow WT, and F Wood E, "Impact of soil moisture aggregation on surface energy flux prediction during SGP97," Geophysical Research Letters, vol. 29(1), 10.1029/2001GL013796, 2002.

[44]. Chen F, Crow WT, Colliander, Cosh MH, Jackson TJ, Bindlish R, Reichle RH, Chan SK, Bosch DD, Starks PJ and Goodrich DC, "Application of triple collocation in ground-based validation of Soil Moisture Active/Passive (SMAP) level 2 data products," IEEE Journal of Selected Topics in Applied Earth Observations and Remote Sensing. vol. 99(1–14), doi:10.1109/JSTARS.2016.2569998. 2016.

[45]. Moghaddam MD, Entekhabi D, Goykhman Y, Li K, Liu M, Mahajan A, Nayyar A, Shuman D, and Teneketzis D, "A wireless soil moisture smart sensor web using physics-based optimal control: concept and initial demonstration," IEEE Journal of Selected Topics in Applied Earth Observations and Remote Sensing, vol. 3, no. 4, pp. 522–535, 12 2010.

[46]. Desilets D, Zreda M, and Ferré TPA, "Nature's neutron probe: Land surface hydrology at an elusive scale with cosmic rays," Water Resour. Res, 46, W11505, doi:10.1029/2009WR008726, 2010.

[47]. Crow WT, Milak S, and Reichle RH, AirMOSS: L4 Modeled Volumetric Root Zone Soil Moisture, 2012–2015, ORNL DAAC, Oak Ridge, Tennessee, USA, 2017.

[48]. Reichle R et al., "Global assessment of the SMAP Level-4 surface and root-zone soil moisture product using assimilation diagnostics," Journal of Hydrometeorology, vol. 18, no. 12, pp. 3217–3237, 10.1175/JHM-D-17-0130.1, 2017. [PubMed: 30364509]

[49]. Gruber A, T Crow W, and Dorigo W, "Assimilation of spatially sparse in situ soil moisture networks into a continuous model domain," Water Resources Research, in press, 2018.

[50]. Shi Y, Davis KJ, Zhang F, Duffy CJ, and Yu X, "Parameter estimation of a physically-based land surface hydrologic model using the ensemble Kalman Filter: A synthetic experiment," Water Resources Research, vol. 50, pp. 706–724, 10.1002/2013WR014070, 2014.

[51]. Sadeghi M, Tabatabaeenejad A, Tuller M, Jones SB, and Moghaddam M, "Advancing NASA's AirMOSS P-Band radar root zone soil moisture retrieval algorithm via incorporation of Richards' Equation," Remote Sens, vol. 9, no. 1, 2017.

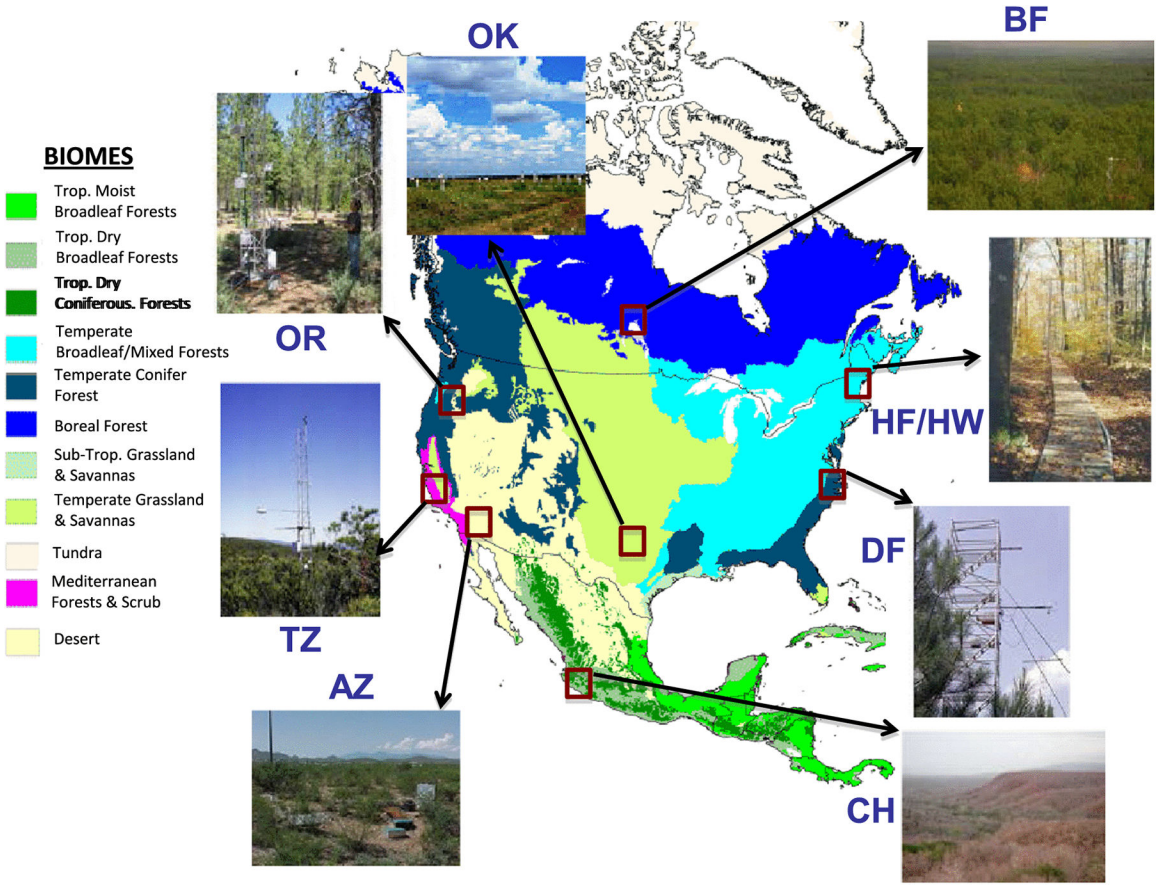

Figure 1.
Map of the AirMOSS experimental site locations utilized here.

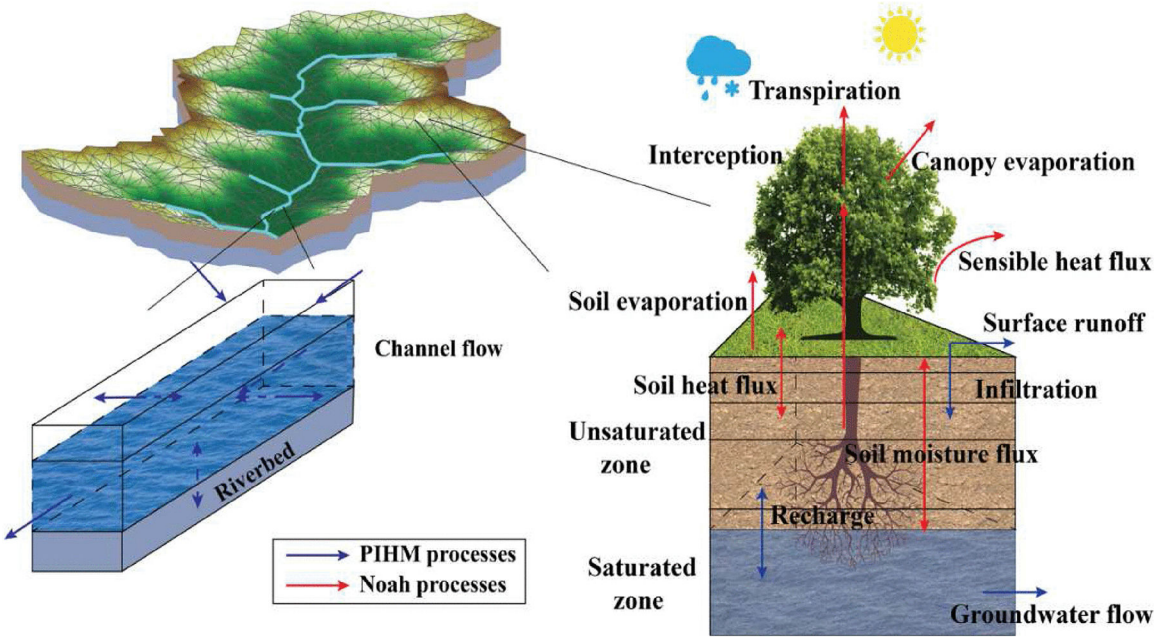

Figure 2.
Description of basic processes represented by Flux-PIHM on each TIN element.

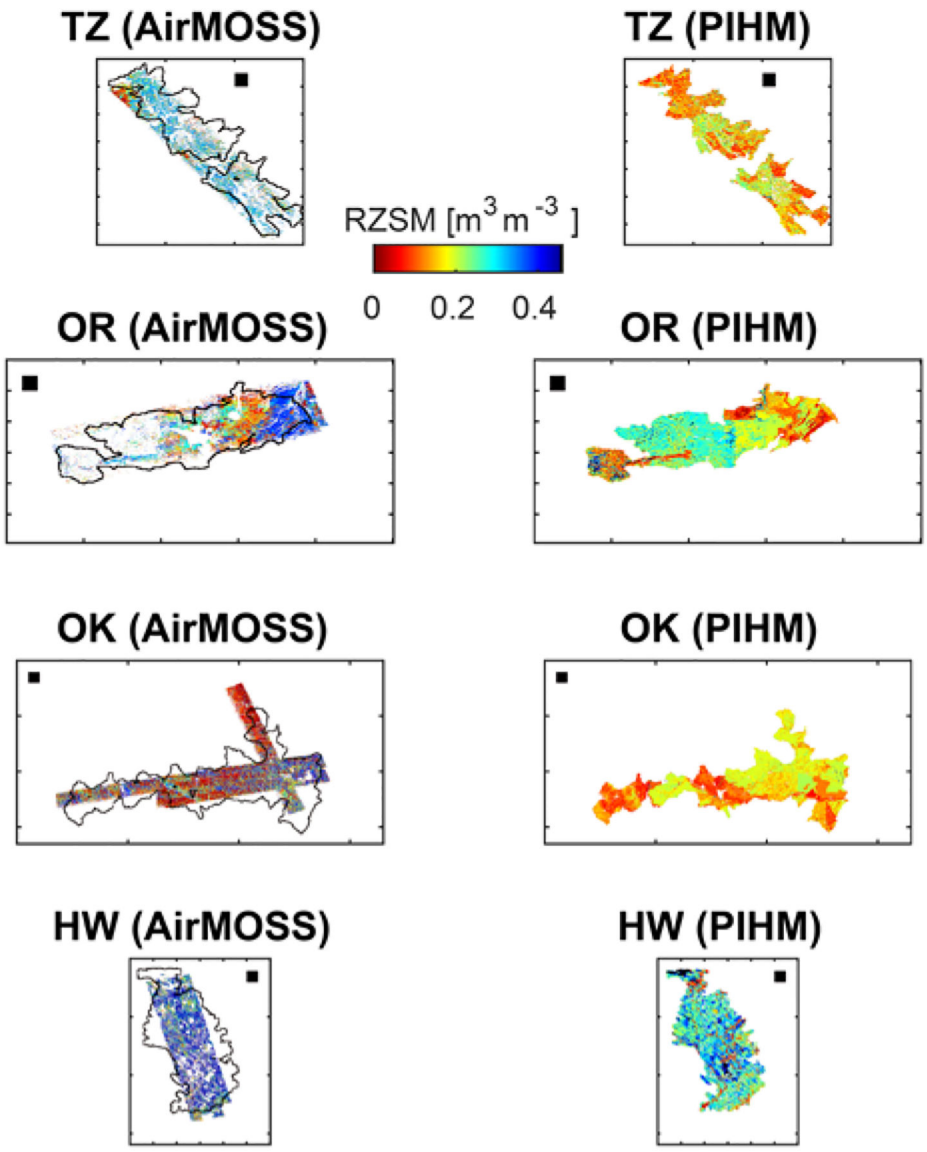

Figure 3a.

3-arc-sec resolution RZSM (0–40 cm) imagery obtained from both AirMOSS L2/3 (left column) and Flux-PIHM (right-column) for: (TZ) 21 Nov. 2013, (OR) 21 Apr. 2013 (OK), 30 Oct. 2012, and (HW) 01 June 2014. The black rectangle is 10 km on a side and plotted for scale reference.

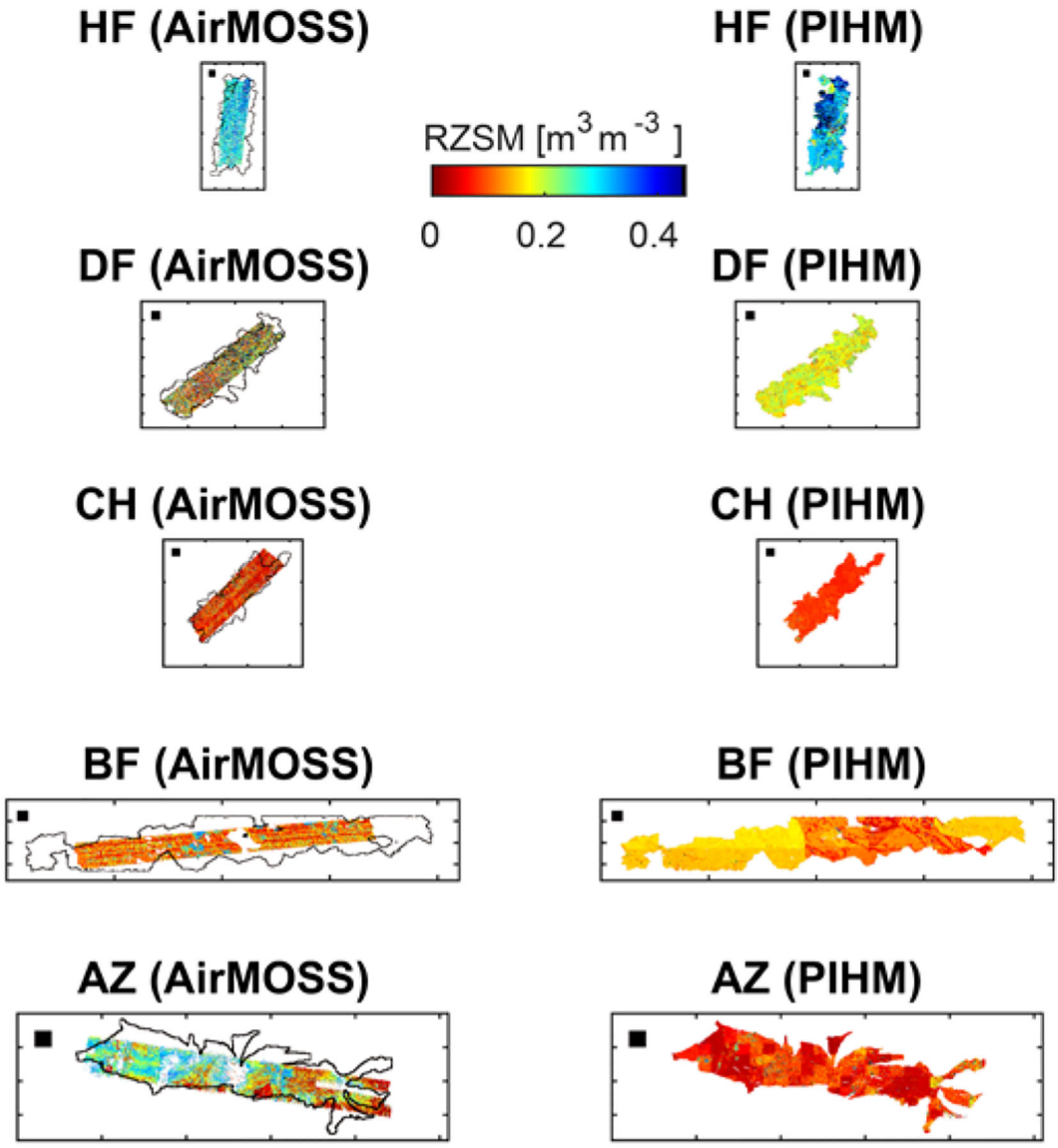

Figure 3b.

3-arc-sec resolution RZSM (0–40 cm) obtained from both AirMOSS L2/3 (left column) and Flux-PIHM (right-column) for: (HF) 21 Oct. 2012, (DF) 22 Oct., 2012, (CH) 30 May 2013, (BR) 11 Oct. 2012, and (AZ) 29 Oct. 2012. The black rectangle is 10 km on a side and plotted for scale reference.

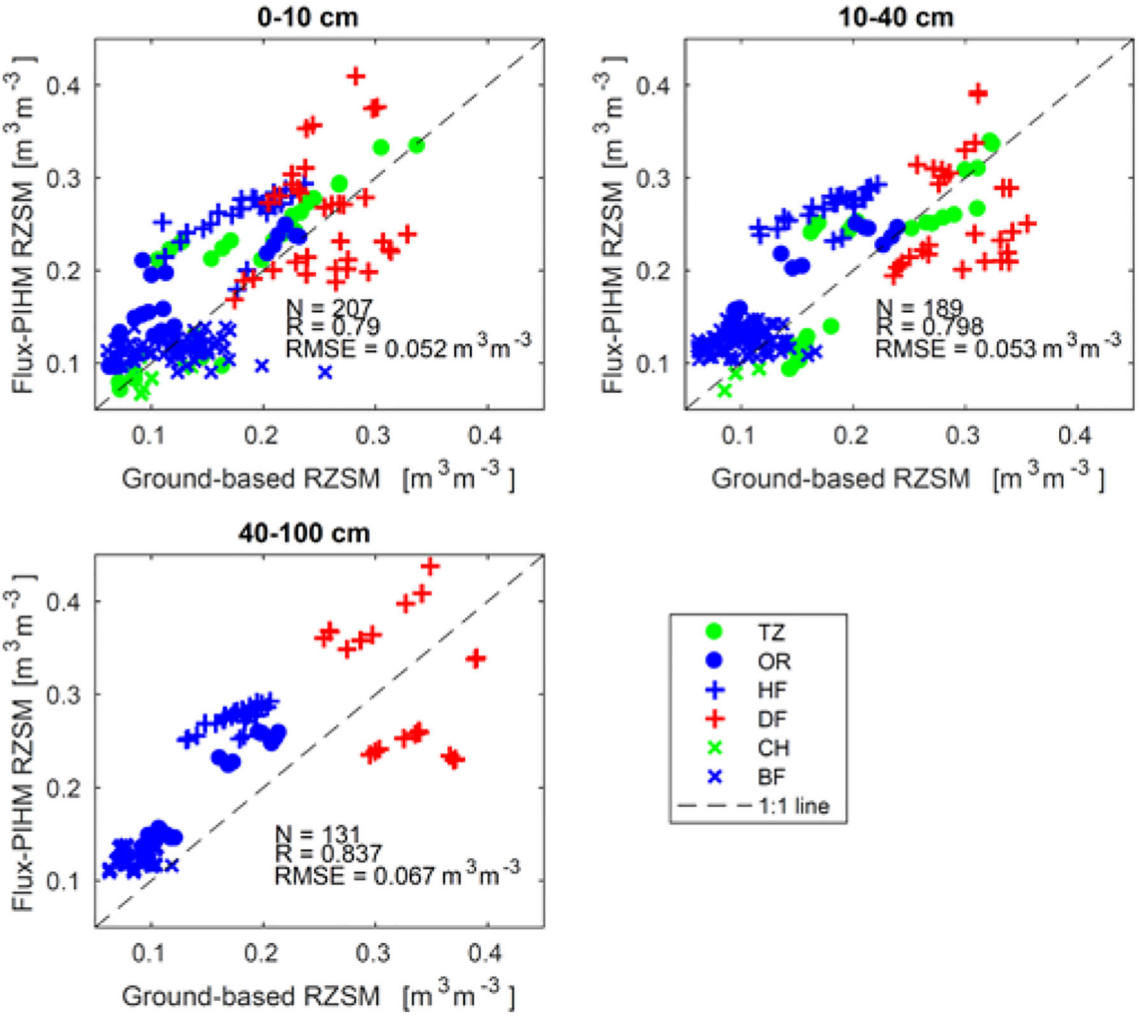

Figure 4.

Scatterplot comparisons between Flux-PIHM a) 0–10 cm, b) 10–40 cm and c) 40–100 cm RZSM predictions and collocated, ground-based RZSM measurements across multiple AirMOSS sites. For consistency with previously-published AirMOSS validation results, each point represents a single AirMOSS over-flight time listed in Table 1.

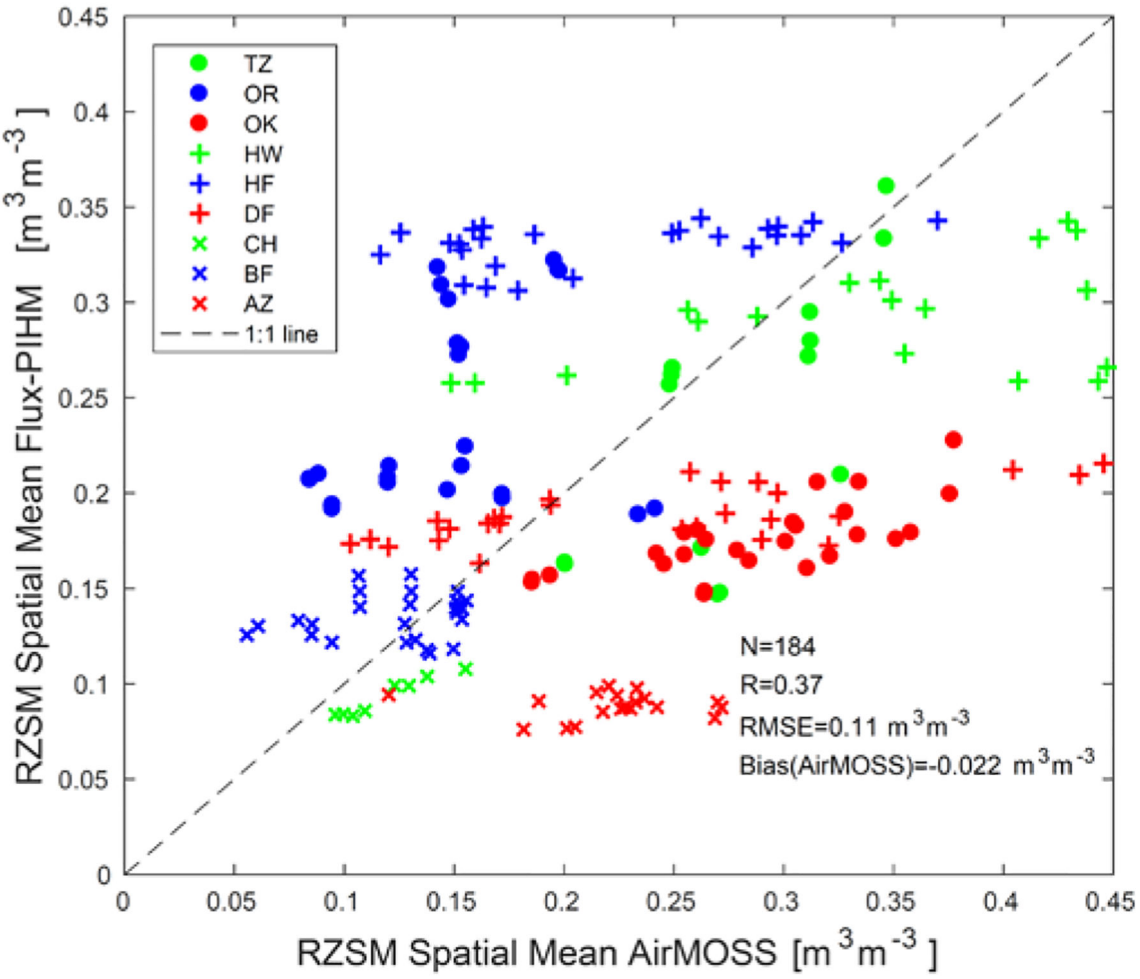

Figure 5.

Scatter-plot of scene-averaged Flux-PIHM and AirMOSS L2/3 RZSM estimates for all nine AirMOSS study sites. Each point represents a spatially-averaged RZSM value acquired during a single AirMOSS over-flight time listed in Table 1.

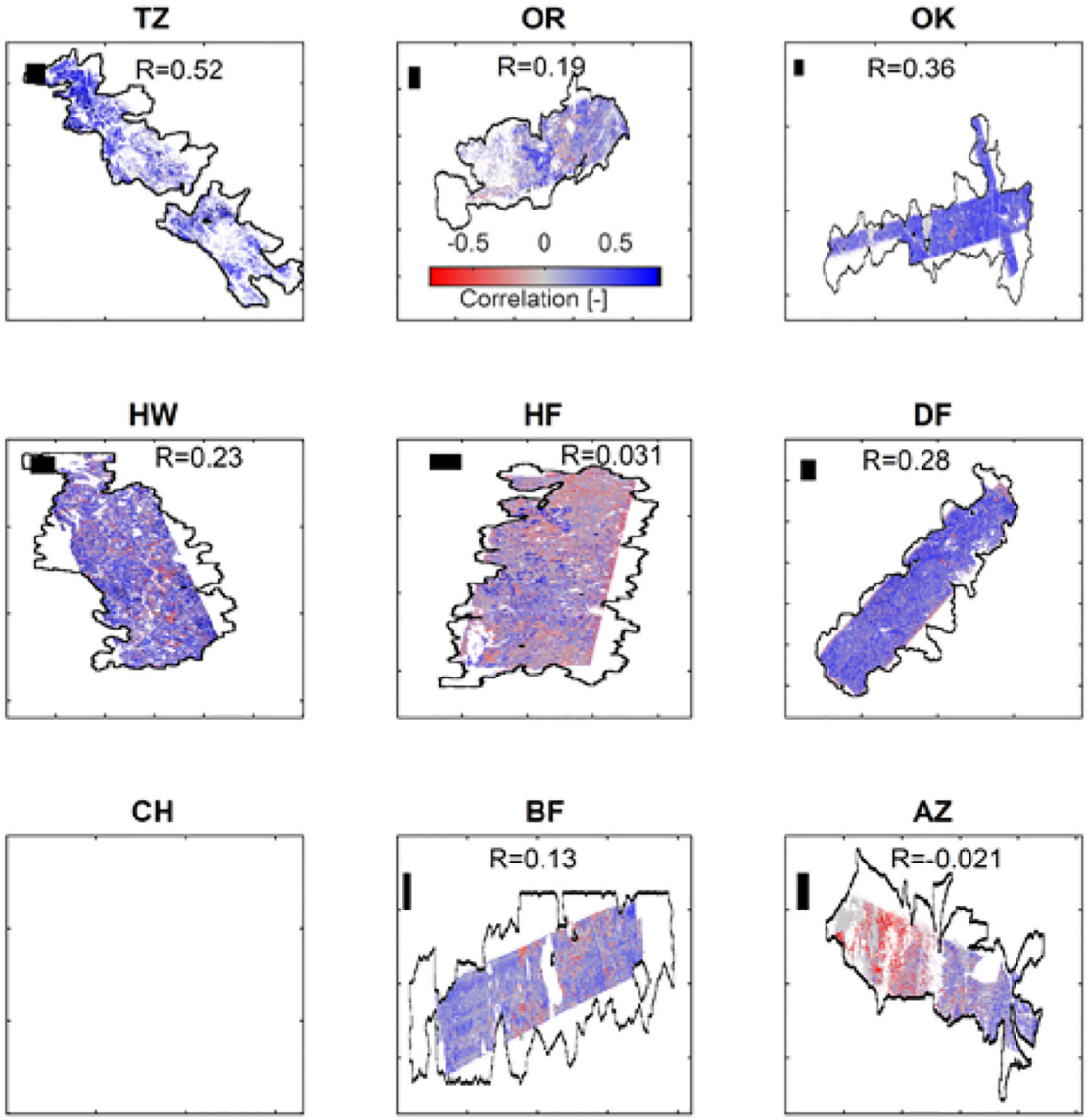

Figure 6.

Temporal correlation between 3-arc-sec, 0–40-cm Flux-PIHM and AirMOSS L2/3 RZSM products for the nine AirMOSS study sites. Areas lacking adequate temporal sampling coverage (including all CH results) are masked in white. The black outline represents the spatial extent of the Flux-PIHM modeling domain at each site. Numbers give the areal average of sampled temporal correlation (R) at each site. The black rectangle is 10 km on a side and plotted for scale reference. Note that the aspect ratios of some images have been modified.

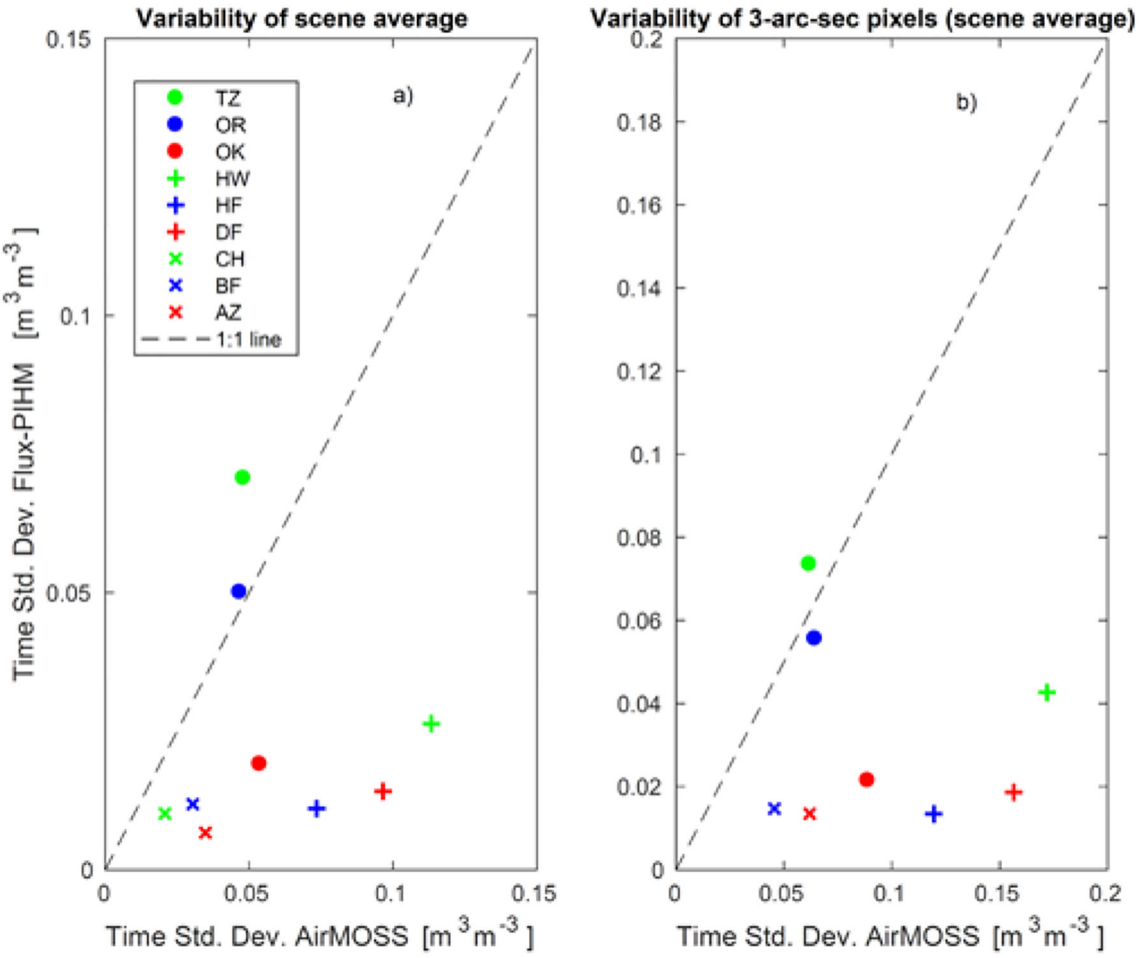

Figure 7.

For all AirMOSS study sites, scatterplots of 0–40-cm Flux-PIHM and AirMOSS L2/3 estimates for a) the temporal standard deviation of scene-averaged RZSM and b) the scene average of the RZSM temporal standard deviation sampled for individual 3-arc-sec pixels.

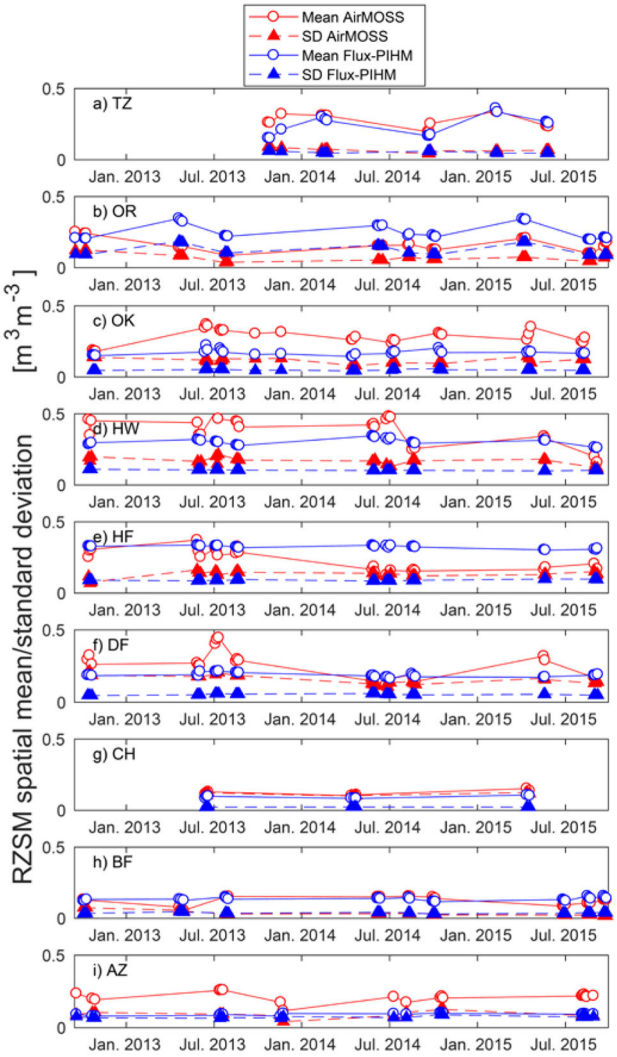

Figure 8.

For both 0–40-cm AirMOSS L2/3 and Flux-PIHM RZSM products, the time series of areal-averaged RZSM (“Mean”) and the within-scene 3-arc-sec RZSM standard deviation (“SD”) for all nine AirMOSS sites.

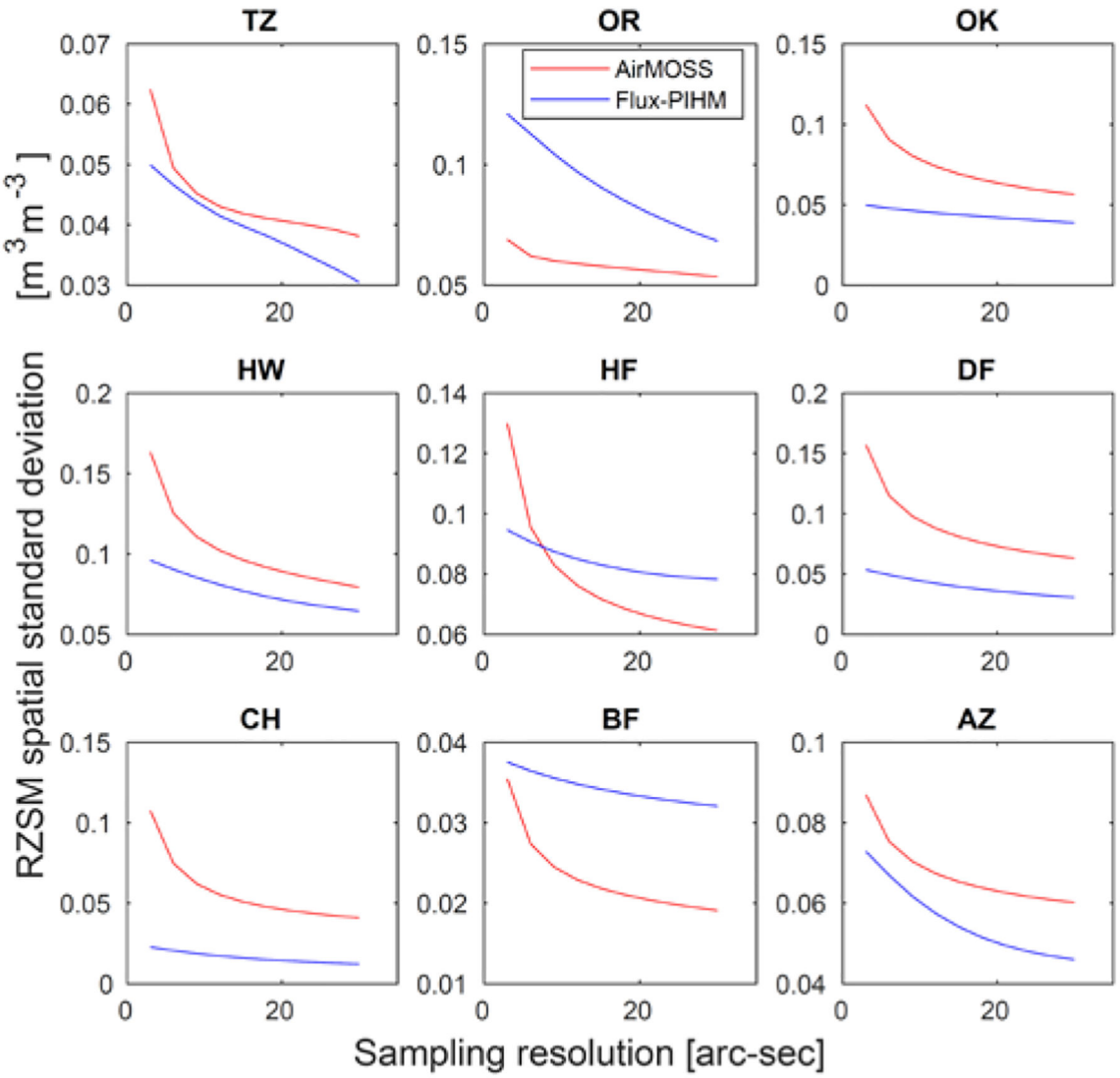

Figure 9.

The sampled spatial standard deviation (averaged across all available AirMOSS over-flight times) for AirMOSS L2/3 and Flux-PIHM 0–40-cm RZSM fields across a range of sampling resolution scales.

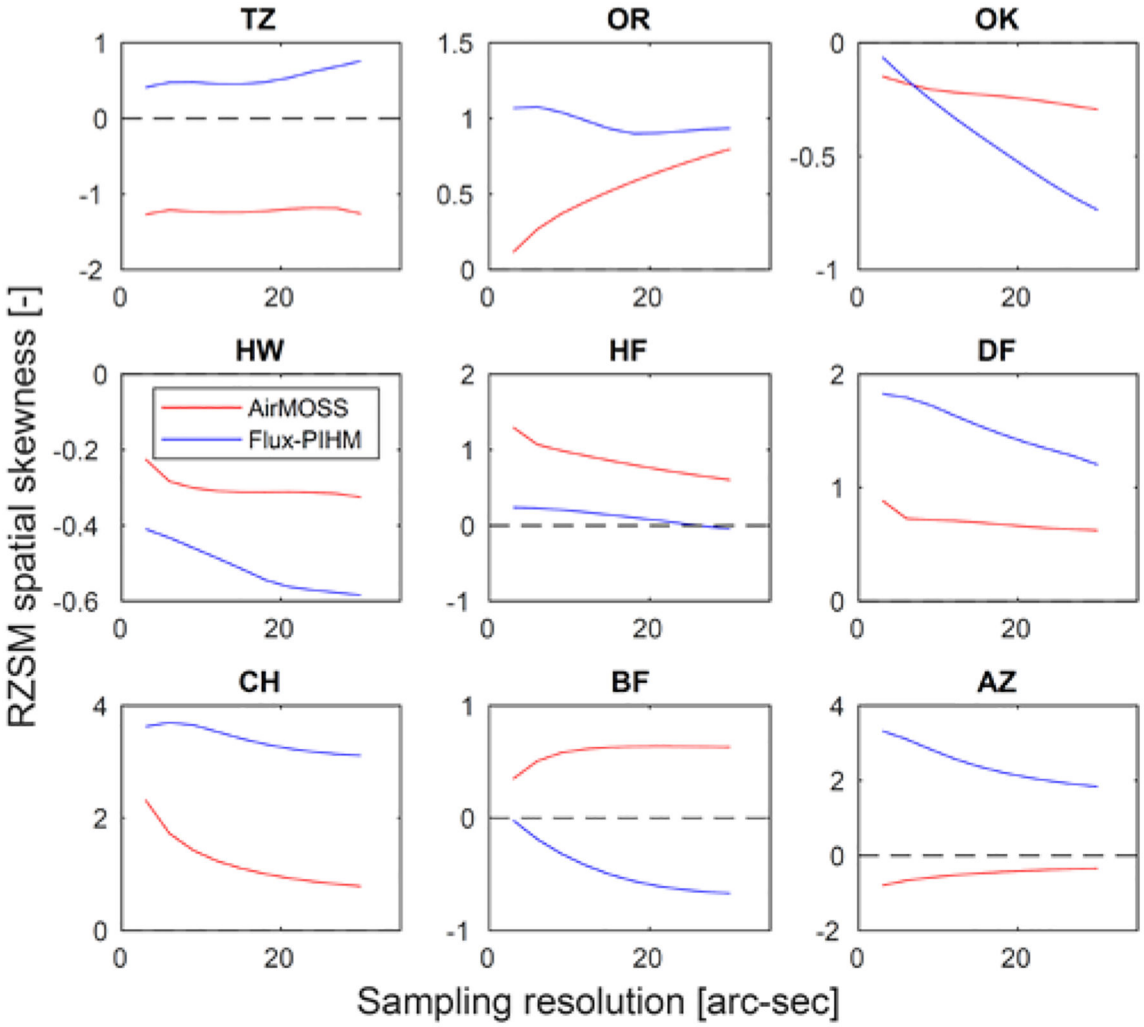

Figure 10.

The sampled spatial skewness (averaged across all available AirMOSS over-flight times) for 0–40-cm AirMOSS L2/3 and Flux-PIHM RZSM fields across a range of sampling resolution scales.

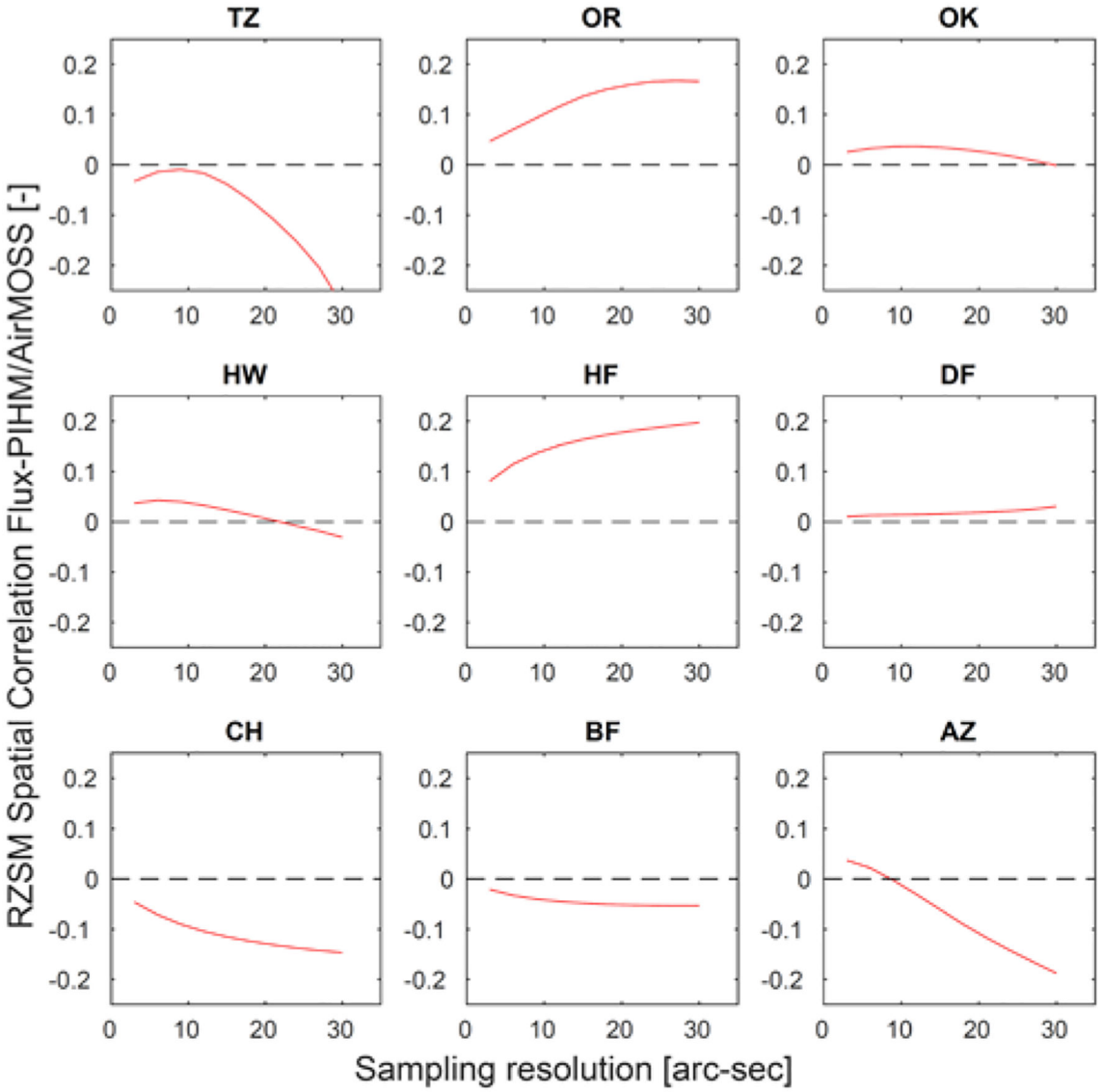

Figure 11.

The static spatial correlation (averaged across all available AirMOSS over-flight times) between 0–40-cm AirMOSS L2/3 and Flux-PIHM RZSM fields across a range of sampling resolution scales.

Table 1.

Name, abbreviations, biome, and aircraft over-flight dates for the 9 AirMOSS experimental sites utilized here.

AirMOSS Site	Biome	Over-flights [Year/Month Day]
Tonzi Ranch (TZ)	Mediterranean Shrubland	20131024, 20131028, 20131121, 20140213,20140220, 20140224, 20140922, 20140925,20140927, 20150210, 20150213, 20150526, 20150528, 20150531
Metolius (OR)	Coniferous Temperature Forest	20120918, 20121007, 20121010, 20130421, 20130425, 20130429, 20130726, 20130729, 20130801, 20140609, 20140612, 20140619, 20140811, 20140814, 20141001, 20141005, 20141008, 20150406, 20150410, 20150413 20150821, 20150824, 20150827, 20150923, 20150926, 20150929
MOISST (OK)	Temperate Grassland	20121024, 20121027, 20121030, 20130614, 20130617, 20130620, 20130716, 20130719, 20130723, 20130927, 20131120, 20140416, 20140418, 20140424, 20140708, 20140711, 20140715, 20141014, 20141017, 20141021, 20150416, 20150420, 20150424, 20150807, 20150811, 20150814
Howland Forest (HW)	Temperate Mixed Forests	20130825, 20140529, 20140601, 20140603, 20140627, 20140702, 20140706, 20140820, 20140823, 20140826, 20150521, 20150524, 20150903, 20150907, 20150909
Harvard Forest (HF)	Temperate Mixed Forest	20121015, 20121018, 20121021, 20130530, 20130602, 20130606, 20130707, 20130710, 20130712, 20130819, 20130822, 20130825, 20140529, 20140601, 20140603, 20140627, 20140702, 20140706, 20140820, 20140823, 20140826, 20150521, 20150524, 20150903, 20150907, 20150909
Duke Forest (DF)	Temperate Coniferous Forest	20121013, 20121017, 20121022, 20130529, 20130601, 20130604, 20130706, 20130709, 20130713, 20130818, 20130821, 20130824,20140527, 20140528, 20140531, 20140604, 20140626, 20140630, 20140705, 20140819, 20140822, 20140827, 20150521, 20150523,20150902, 20150905, 20150910
Chamela (CH)	Subtropical Forest	20121015,20121018,20121021,20130530,20130602, 20130606,20130707,20130710,20130712,20130819, 20130822
BERMS (BF)	Boreal Forest	20121004, 20121007, 20121011, 20130422, 20130426, 20130501, 20130727, 20130729, 20130802, 20140608, 20140611, 20140614, 20140812, 20140815, 20141001, 20141004, 20141007, 20150629, 20150702 20150705, 20150819, 20150823, 20150826 20150922, 20150925, 20150928
Walnut Gulch (AZ)	Desert Shrubland	20120920, 20121023,20121029, 20130715, 20130718, 20130722,20131119, 20131125, 20140712, 20140808, 20141018, 20141021, 20141024, 20150808, 20150810, 20150813, 20150816, 20150818, 20150901